Article

Computational Studies on Holey TMC$_6$ (TM = Mo and W) Membranes for H$_2$ Purification

Juan Xie [1,2,†], **Cai Ning** [3,†] , **Qinqin Liu** [1], **Zhongti Sun** [1,*], **Juan Yang** [1,*] and **Huilong Dong** [2,*]

1   School of Materials Science and Engineering, Jiangsu University, Zhenjiang 212013, China; xiejuan@cslg.edu.cn (J.X.); qqliu@ujs.edu.cn (Q.L.)
2   School of Materials Engineering, Changshu Institute of Technology, Changshu 215500, China
3   School of Physics, Southeast University, Nanjing 211189, China; caining54@njust.edu.cn
*   Correspondence: ztsun@ujs.edu.cn (Z.S.); yangjuan6347@mail.ujs.edu.cn (J.Y.); huilong_dong@126.com or hldong@cslg.edu.cn (H.D.)
†   These authors contributed equally to this work.

Abstract: The purification of hydrogen (H$_2$) has been a vital step in H$_2$ production processes such as steam–methane reforming. By first-principle calculations, we revealed the potential applications of holey TMC$_6$ (TM = Mo and W) membranes in H$_2$ purification. The adsorption and diffusion behaviors of five gas molecules (including H$_2$, N$_2$, CO, CO$_2$, and CH$_4$) were compared on TMC$_6$ membranes with different phases. Though the studied gas molecules show weak physisorption on the TMC$_6$ membranes, the smaller pore size makes the gas molecules much more difficult to permeate into h-TMC$_6$ rather than into s-TMC$_6$. With suitable pore sizes, the s-TMC$_6$ structures not only show an extremely low diffusion barrier (around 0.1 eV) and acceptable permeance capability for the H$_2$ but also exhibit considerably high selectivity for both H$_2$/CH$_4$ and H$_2$/CO$_2$ (>10^{15}), especially under relatively low temperature (150–250 K). Moreover, classical molecular dynamics simulations on the permeation process of a H$_2$, CO$_2$, and CH$_4$ mixture also validated that s-TMC$_6$ could effectively separate H$_2$ from the gas mixture. Hence, the s-MoC$_6$ and s-WC$_6$ are predicted to be qualified H$_2$ purification membranes, especially below room temperature.

Keywords: carbon-based membrane; hydrogen purification; first-principle calculations; selectivity

1. Introduction

With the increasing environmental pollution issues and global energy crisis, more and more attention has been paid to green energy resources, particularly hydrogen (H$_2$) energy [1,2]. Though lots of methods have been developed, steam–methane reforming is still the main approach for industrial production of H$_2$ [3]. During the steam–methane reforming process, however, the mixture composed of H$_2$, CO$_2$, and CH$_4$ is inevitable, which renders the purification of H$_2$ highly crucial in hydrogen production. The membrane separation technology is one of the most widely accepted methods for H$_2$ separation and purification [4]. Among the reported membranes, two-dimensional (2D) carbon-based membranes have been extensively studied due to their distinct advantages, e.g., low energy consumption and good cyclicity through physical interactions [5–7].

Material design by computational methods has been an effective tool to achieve novel 2D carbon-based ultrathin membranes for H$_2$ separation and purification, especially for the ones with intrinsic pores. As one of the most well-known representatives, the porous graphitic carbon nitride (g-C$_3$N$_4$) monolayer has received a lot of attention for its potential as an effective gas separation membrane. Under room temperature, g-C$_3$N$_4$ could exhibit extremely high theoretical selectivity for H$_2$/CH$_4$ in the order of 10^{46} [8]. Moreover, further theoretical simulations indicated that g-C$_3$N$_4$ is also capable in helium (He) purification from both natural gas and noble gas molecules [9]. With the help of theoretical simulations, the porous C$_2$N monolayer was reported to be suitable for He

separation from other gases (Ne, CH_4, CO_2, etc.) [10]. Wang et al. investigated the diffusion properties of He, Ne, CO_2, Ar, N_2, CO, and CH_4 through a porous monolayer covalent triazine-based framework (CTF) membrane. Calculation results demonstrate that the selectivity for He and H_2 against common gas molecules (such as CO_2, N_2, CO, and CH_4) is highly promising for practical applications [11]. Meng et al. theoretically explored the structural and mechanical properties of metal-free fused-ring polyphthalocyanine (H_2PPc) and halogenated H_2PPc (F-H_2PPc and Cl-H_2PPc) membranes. It was found that fluorination and chlorination can effectively tune the permeable pores. Particularly, F-H_2PPc is fascinating as a separation membrane for H_2 purification [12]. Recently, a series of 2D γ-C_4X (X = O, S, or Se) membranes with intrinsic pores were theoretically designed, among which γ-C_4O shows both low diffusion barriers (0.35 eV) and high permeance (5.0×10^{-7} mol m^{-2} s^{-1} Pa^{-1}) for H_2. Moreover, γ-C_4O is highly promising as a H_2 purification membrane from the H_2/CH_4 mixture with a selectivity of about 10^{19} [13]. The existing studies indicate that there are abundant possibilities for carbon-based ultrathin membranes with intrinsic pores. Therefore, carbon-based membranes with different pore sizes and termination on the pore edges are indispensable for H_2 purification.

Besides the ones entirely composed of non-metal elements, 2D membranes composed of carbon and metal atoms may also play a vital role as gas separation membranes due to the incorporation of metal atoms. In the pioneering work by Li et al., a novel 2D transition metal carbide (h-TMC_6, TM = Mo, W) structure was theoretically designed [14]. It was found that the crystal structure of h-TMC_6 belongs to the hexagonal Kagome lattice. The stability of h-TMC_6 was confirmed by molecular dynamics simulations and phonon spectra calculations. Later, Liu et al. reported other transition-metal carbides with the same composition of TMC_6 (TM = Mo, W) but a tetragonal lattice [15], therefore being named s-TMC_6. In general, the TMC_6 monolayers show triple atomic layer structures with Mo/W atomic layers sandwiched between two carbon atomic layers, with TM atoms coordinated with six nearest neighboring C atoms. More importantly, in both h-TMC_6 and s-TMC_6, there are intrinsic pores surrounded by the TM atoms and carbon atoms, whose sizes are mainly determined by the lattice structures.

In this work, the capability of holey structures of TMC_6 (M = Mo, W) membranes for H_2 purification was theoretically explored, both square and hexagonal phases. By comparing the pore size and separation performance against H_2 and other gas molecules (N_2, CO, CO_2, CH_4), it was found that s-TMC_6 is more promising for H_2 purification, especially from H_2/(CO_2, CH_4) mixtures below room temperature (150–250 K). Our work not only predicts the potential applications of the TMC_6 membranes but also recommends the novel membrane materials for H_2 purification under low temperature.

2. Computational Methods

The Vienna *ab initio* simulation package (VASP) [16,17] was used for the first-principle calculations with plane-wave basis set and the projector augmented-wave (PAW) [18] method. The Perdew–Burke–Ernzerhof (PBE) [19] functional was adopted, with a cutoff energy of 500 eV. The structural relaxations were considered to be converged until the change in total energy reaches 10^{-5} eV and the residual force per atom reaches 0.02 eV Å^{-1}. To avoid the interaction between the neighboring periodic images, a vacuum slab around 2 nm was applied for all the structures. The Brillouin zone was sampled with Monkhorst–Pack [20] k-point grids of $11 \times 11 \times 1$ and $5 \times 5 \times 1$ for unit cell of h-TMC_6 and s-TMC_6, respectively. Furthermore, $4 \times 4 \times 1$ k-point grids were adopted for the 3×3 supercell of h-TMC_6, while $3 \times 3 \times 1$ k-point grids were adopted for the 2×2 supercell of s-TMC_6. For accurate description of weak van der Waals (vdW) interactions, Grimme's dispersion correction (DFT–D3) was included during the adsorption-related calculations [21]. The climbing image nudged elastic band (CI-NEB) method [22] was used to search the minimum energy pathway (MEP) and confirm the transition state (*TS*) during the diffusion of gas molecules. The diffusion barriers (E_b) were calculated to evaluate the capability of gas

molecules passing through the intrinsic pores in the TMC$_6$ membranes by the following definition:

$$E_b = E_{TS} - E_{IS} \tag{1}$$

where the E_{TS} and E_{IS} denote the energy of transition state (*TS*) and initial state (*IS*), respectively. Additionally, the adsorption energies (E_{ad}) of gas molecules on 2D TMC$_6$ were calculated by

$$E_{ad} = E_{mol*} - E_{mol} - E_* \tag{2}$$

where E_{mol*}, E_{mol}, and E_* stand for the energy of adsorption system, isolated molecule, and 2D TMC$_6$, respectively. Herein, a negative E_{ad} value means that the adsorption is favorable as exothermic process.

The classical molecular dynamics (MD) simulations on permeation process of H$_2$, CO$_2$, and CH$_4$ mixture were implemented by Forcite module available in the Materials Studio software package. Gas molecules were interspersed between the TMC$_6$ membranes, and the initial condition was 250 K with a total simulation time of 5000 ps. The NVT ensemble and universal force field [23] were employed during the simulation with a time step of 1 fs.

3. Results and Discussion

As predicted in previous work, the single-layered TMC$_6$ (M = Mo, W) includes two different phases with holey structure, namely, the square phase (s-TMC$_6$) and the hexagonal phase (h-TMC$_6$). s-TMC$_6$ shows *P4/mbm* symmetry with a lattice constant of 8.541 and 8.543 Å for s-MoC$_6$ and s-WC$_6$, respectively. There are 4 TM atoms and 24 carbon atoms in the unit cell of s-TMC$_6$. Due to the extremely close lattice parameters, s-MoC$_6$ and s-WC$_6$ exhibit intrinsic pores with the same diameter of about 5.65 Å, which were obtained by directly measuring from the optimized atomic positions of carbon in the edge of pores. The intrinsic pores are composed of four TM atoms and eight C atoms, as displayed in Figure 1a. Differently, the h-TMC$_6$ exhibits *P6̄m2* symmetry with the lattice constant of 4.381 and 4.383 Å for h-MoC$_6$ and h-WC$_6$, respectively. The unit cell of h-TMC$_6$ contains one TM atom and six carbon atoms. Due to the more compact atomic configurations of h-TMC$_6$, their intrinsic pores have smaller sizes when compared with s-TMC$_6$. As indicated in Figure 1b, the pores in h-TMC$_6$ are composed of three TM atoms and six C atoms, whose diameters are about 4.48 Å.

After the confirmation of pore structures in the 2D TMC$_6$, we then tested their performance in gas adsorption and diffusion. In this work, five different kinds of gas molecules (containing H$_2$, N$_2$, CO, CO$_2$, and CH$_4$) were tested, which are the main components of the gas mixture in the steam–methane reforming process. All the adsorption configurations of gas molecules were fully relaxed. The adsorption energies (E_{ad}), equilibrium adsorption heights (h), and diffusion barriers (E_b) are systematically summarized in Table 1. In the equilibrium configurations, the adsorption heights between the gas molecules and substrate are mostly in the range of 2.0–2.5 Å, along with adsorption energies within −0.18 eV, as shown in Figure 2a,b. The large adsorption heights and weak adsorption strength evidently indicate physisorption through van der Waals interaction between the gas molecules and TMC$_6$ substrates. Generally speaking, the E_{ad} of the same gas molecule on MoC$_6$ and WC$_6$ is almost the same, implying the negligible influence of TM atoms on the gas adsorption. Meanwhile, the E_{ad} values of a gas molecule on s-TMC$_6$ will be slightly smaller than those on h-TMC$_6$. However, it is interesting to see that the diffusion of the same molecule on h-TMC$_6$ will be much more difficult than that on s-TMC$_6$ due to the much greater E_b values (see Figure 2c). Another finding is that for s-MoC$_6$ and s-WC$_6$, due to the relatively small E_b values, the difference between E_b of the same gas molecule on them is also very small (<0.1 eV). For h-MoC$_6$ and h-WC$_6$, a significant difference between E_b of the same gas molecule on them arises (up to 0.33 eV). Therefore, though the gas molecules have close adsorption interaction on the TMC$_6$ membranes, their diffusion performance is highly distinguished.
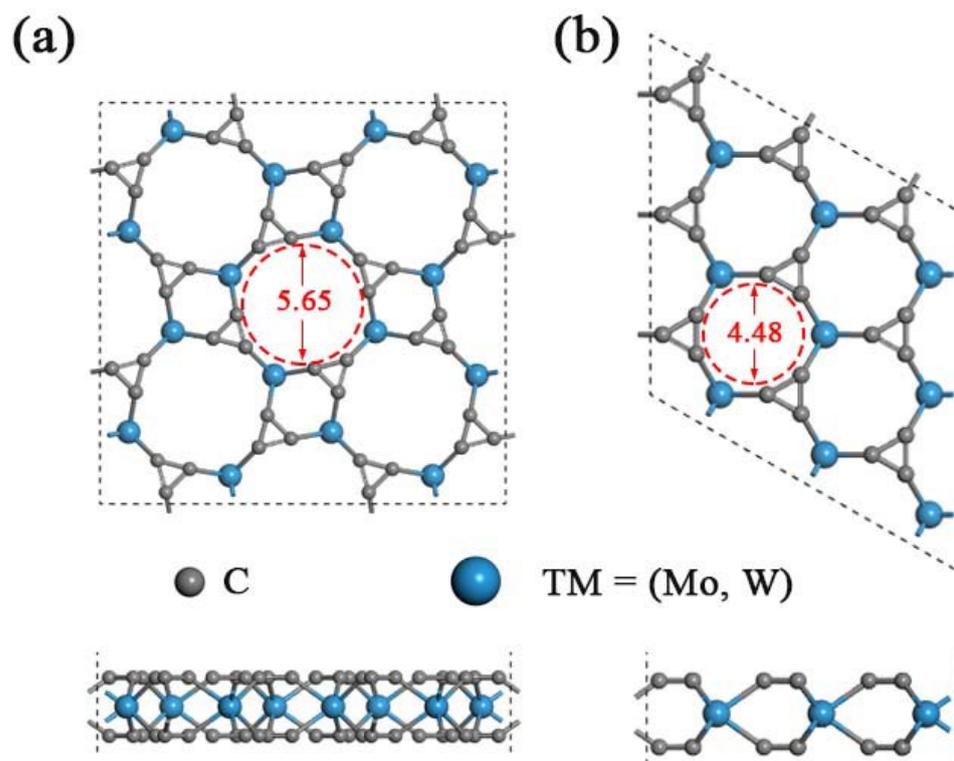
Figure 1. Schematic illustrations of TMC_6 (top view and side view) supercells: (**a**) Square transition-metal carbides s-TMC_6; (**b**) hexagonal transition-metal carbides h-TMC_6. The gray and blue balls represent C and TM atoms, respectively.

Table 1. The adsorption energies (E_{ad}, eV), equilibrium adsorption heights (h, Å), diffusion barriers for the studied gases (H_2, N_2, CO, CO_2, and CH_4) passing through the intrinsic pore (E_b, eV) of 2D TMC_6, energy differences (ΔE_{sub}, eV) of the TMC_6 membranes between free-standing state and TS without adsorbates, the bond lengths (l_1 and l_2, Å) of the gas molecules with free-standing state and TS.

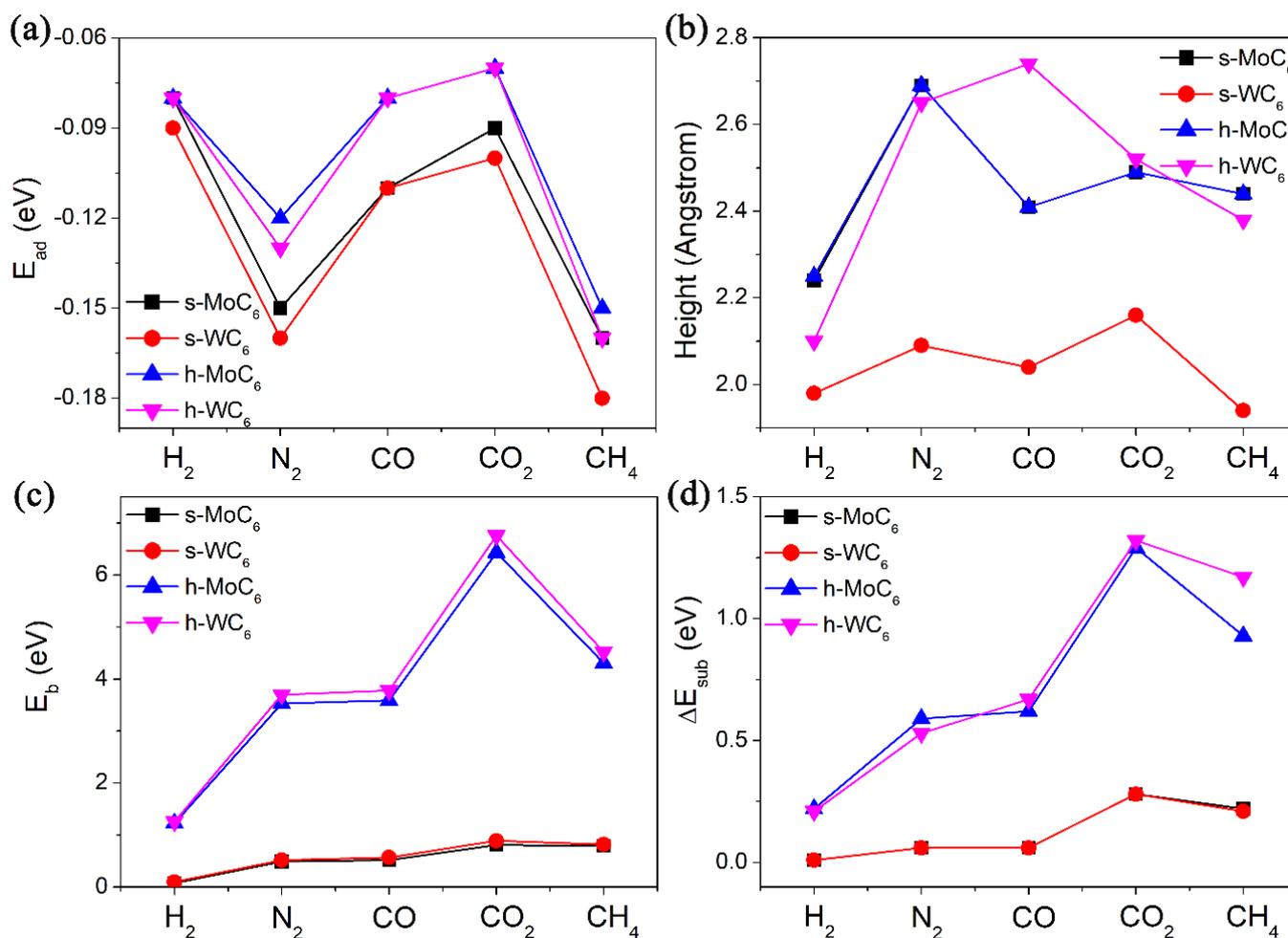|	Property	H_2	N_2	CO	CO_2	CH_4
s-MoC_6	E_{ad}	−0.08	−0.15	−0.11	−0.09	−0.16
	h	2.24	2.69	2.41	2.49	2.44
	E_b	0.08	0.49	0.52	0.81	0.79
	ΔE_{sub}	0.01	0.06	0.06	0.28	0.22
	l_1	0.75	1.11	1.14	1.18	1.10
	l_2	0.75	1.12	1.15	1.18	1.10
s-WC_6	E_{ad}	−0.09	−0.16	−0.11	−0.10	−0.18
	h	1.98	2.09	2.04	2.16	1.94
	E_b	0.10	0.52	0.57	0.89	0.82
	ΔE_{sub}	0.01	0.06	0.06	0.28	0.21
	l_1	0.75	1.11	1.14	1.18	1.10
	l_2	0.75	1.12	1.15	1.18	1.10
h-MoC_6	E_{ad}	−0.08	−0.12	−0.08	−0.07	−0.15
	h	2.25	2.69	2.41	2.49	2.44
	E_b	1.23	3.53	3.59	6.43	4.31
	ΔE_{sub}	0.22	0.59	0.62	1.29	0.93
	l_1	0.75	1.11	1.14	1.18	1.10
	l_2	0.74	1.15	1.18	1.18	1.10
h-WC_6	E_{ad}	−0.08	−0.13	−0.08	−0.07	−0.16
	h	2.10	2.65	2.74	2.52	2.38
	E_b	1.26	3.70	3.78	6.76	4.52
	ΔE_{sub}	0.21	0.53	0.67	1.32	1.17
	l_1	0.75	1.11	1.14	1.18	1.10
	l_2	0.74	1.15	1.18	1.19	1.10

Figure 2. (**a**) The adsorption energies (E_{ad}, eV), (**b**) equilibrium adsorption heights (h, Å), (**c**) diffusion barriers for the studied gases (H_2, N_2, CO, CO_2, and CH_4) passing through the intrinsic pore (E_b, eV) of 2D TMC_6, and (**d**) energy differences (ΔE_{sub}, eV) of the TMC_6 membranes between free-standing state and TS without adsorbates.

After the comparison of adsorption and diffusion performance of different gas molecules on 2D TMC_6, we then turned to the microscopic insights. As displayed in Figure 3, the electron density isosurfaces of H_2, N_2, CO, CO_2, and CH_4 at their corresponding transition states are provided with the same isosurface value of 0.015 e Å^{-3}. For s-TMC_6, it is evident that the smaller pores are fully occupied by the electron density isosurfaces, and the unoccupied parts only appear in larger pores with square shapes. Meanwhile, for h-TMC_6, the triangle shapes appear in the pores as unoccupied parts, whose area is significantly smaller than that in s-TMC_6. As we can see, under the transition states, there is significant overlapping between the electron density distribution of h-TMC_6 and gas molecules, while the overlapping between s-TMC_6 and gas molecules is lower, especially for H_2, N_2, CO, and CO_2. The overlapping of electron density distribution will cause significant electrostatic interactions. The electrostatic interaction plays a leading part during the permeation process because higher overlapping of electron density distribution corresponds to larger E_b values. In this work, the electrostatic interaction mainly originates from the different pore sizes of 2D TMC_6. As a useful tool to quantitatively understand the selectivity of TMC_6 against different gases, a comparison between the measured diameters of the cross section in the van der Waals (vdW) surface (D_c) of different gas molecules and the pore size of unoccupied vdW surface in 2D TMC_6 was also performed. As measured, the unoccupied vdW diameters of pore in s-MoC_6 and s-WC_6 are 2.29 and 2.32 Å, significantly higher than those of g-C_3N_4 (about 1.70 Å) [8] which results in significantly smaller E_b values for gas

molecules permeating g-C_3N_4 when compared with s-TMC_6. As reported, the D_c of H_2, N_2, CO, CO_2, and CH_4 is 2.44, 3.20, 3.46, 3.44, and 3.78 Å, respectively. Therefore, the pore size of s-TMC_6 is very close to the D_c of H_2 but much smaller than those of N_2, CO, CO_2, and CH_4. This finding means that s-TMC_6 will have considerable selectivity against H_2, attributed to the suitable pore size. Notably, though the pore size of s-WC_6 is slightly larger than that of s-MoC_6, it causes higher E_b for the same gas molecule. Hence, the metal species has relatively less influence on the diffusion of gas molecules, but it is not negligible. In the meantime, the unoccupied vdW diameters of pore in h-TMC_6 are 0, which explains why h-TMC_6 exhibits very high diffusion barriers for all the studied gas molecules.
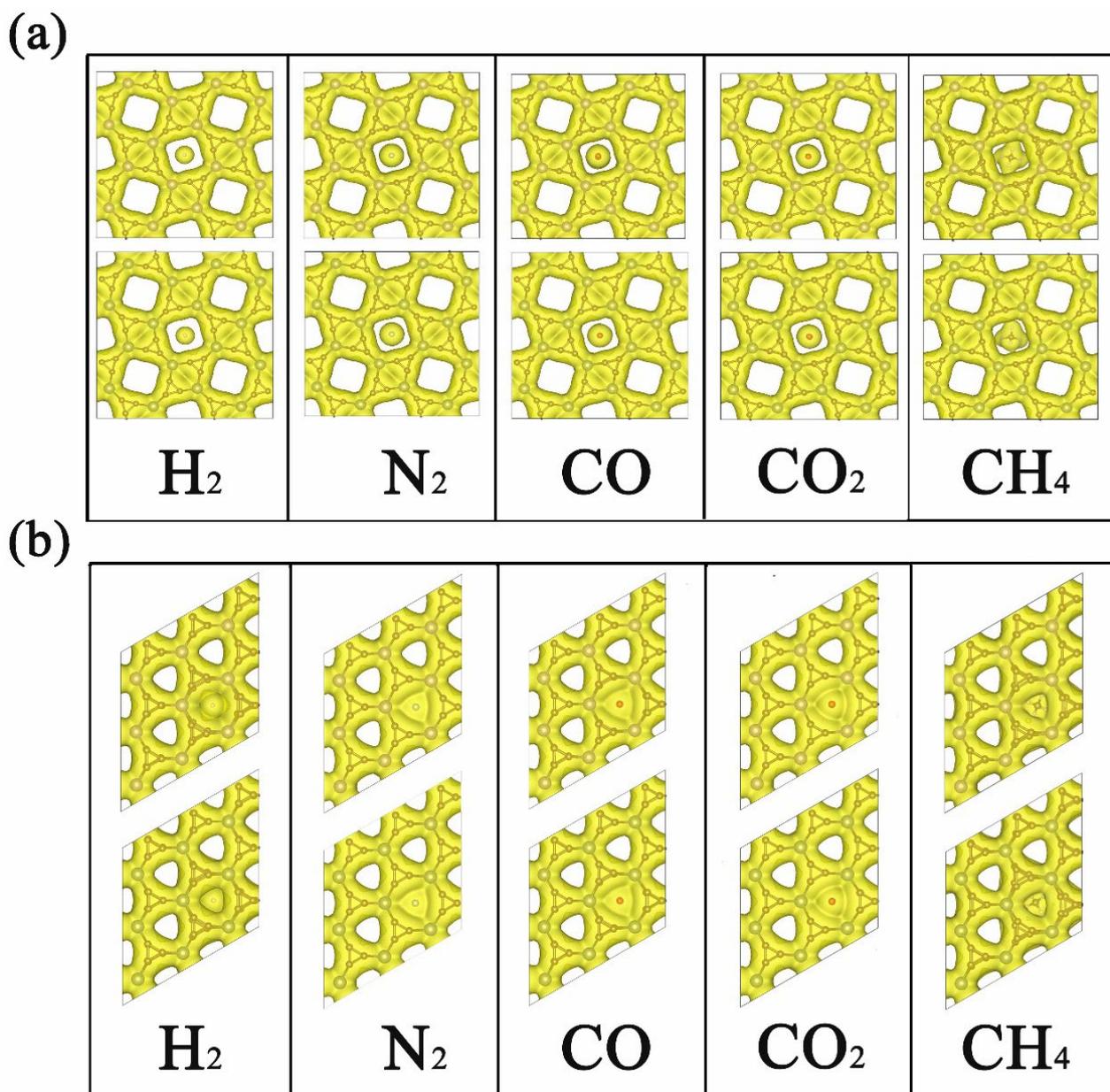

Figure 3. Electron density isosurfaces of H_2, N_2, CO, CO_2, and CH_4 on (**a**) s-TMC_6 and (**b**) h-TMC_6 at their corresponding transition states (TSs). The upper panels mark MoC_6, while the lower panels denote WC_6. The isosurface value is 0.015 e Å^{-3}.

In addition to the comparison between pore sizes, the steric deformation of 2D TMC_6 caused by electrostatic repulsion was also checked. We measured the main bond lengths of different molecules in isolated state (l_1) and TS (l_2), that is, H-H bond length for H_2, N-N

bond length for N_2, C-O bond length for CO and CO_2, and C-H bond length for CH_4, taking in consideration the non-polarized structures of CO_2 and CH_4. The comparison between l_1 and l_2 (seeing Table 1) indicates that the structural changes of the gas molecules under TS are negligible, except for CO and N_2 on h-TMC$_6$. Then, by removing the gas molecule in its TS structure and calculating the single-point energy (SPE) of the 2D TMC$_6$, we can obtain the energy differences (ΔE_{sub}) of the 2D TMC$_6$ between free-standing state and TS without adsorbates, as listed in Table 1. It can be summarized that the ΔE_{sub} is directly proportional to the corresponding E_b. For H_2, N_2, and CO, the electrostatic repulsion takes the proportion of 10–18% in the E_b, and the proportion increases to 20–30% for CO_2 and CH_4. It is revealed that CO_2 and CH_4 have more significant electrostatic repulsion with the pore edge of 2D-TMC$_6$ when compared with other smaller gas molecules. Moreover, as indicated by Figure 2d, the ΔE_{sub} in CO_2 involved TS is obviously larger than that in the corresponding CH_4 involved TS, implying stronger electrostatic repulsion of CO_2 to the substrate. This finding explains the origin of the high E_b values of CO_2 permeating into the pores of 2D TMC$_6$.

To evaluate the gas separation performance quantitatively, we calculated the permeability and selectivity based on diffusion energy barriers. For the permeability, gas kinetic theory was employed under the ideal gas approximation. Herein, the permeance (P, in mol m^{-2} s^{-1} Pa^{-1}) of the penetrated gases is determined by [12]

$$P = \frac{A_p N \int_{v_b}^{\infty} f(v)dv}{A_m \Delta p N_A} = \frac{A_p}{A_m} \frac{p}{\Delta p} \frac{1}{N_A \sqrt{2\pi m k_B T}} \int_{v_b}^{\infty} f(v)dv \tag{3}$$

In Equation (1), A_p denotes the area of the pores, and the total number of collisions per unit time per area (N) is described as $N = \frac{p}{2\pi m k_B T}$, where p, m, k_B, and T stand for pressure, the mass of the molecule, the Boltzmann constant, and temperature, respectively. Hence, $A_\mathrm{p}N$ could be viewed as the number of molecules that collide with the pore area per unit time. The portion of molecules with a speed large enough to overcome the diffusion barrier through the pore (i.e., $v > v_b = \sqrt{\frac{2E_b}{m}}$) is counted as the penetrant portion. A_m, Δp, and $f(v)$ represent the total area of the membrane, the pressure difference (absolute value) between the two sides of the membrane, and the Maxwell velocity distribution, respectively. It is worth noting that A_m is explicit for a 2D membrane, while A_p is related to the pore shapes and the effective radii (R_eff) of the atoms at the pore rim. Here, R_eff is calculated as $R_\mathrm{eff} = R_\mathrm{vdw}/\sqrt{2}$, where R_vdW denotes the vdW radius. The feed pressure and the pressure difference are $p = 3 \times 10^5$ Pa and $\Delta p = 10^5$ Pa as provided in previous work [24].

The calculated permeance vs. temperature for H_2, N_2, CO, CO_2, and CH_4 passing through the intrinsic pore of s-TMC$_6$ and h-TMC$_6$ are displayed in Figure 4. The green dashed line indicates the industrially acceptable permeance capability for gas separation (green dashed line, 6.7×10^{-9} mol m^{-2} s^{-1} Pa^{-1}). Over the temperature range of 100–500 K, the permeance values for each gas molecule through s-TMC$_6$ are evidently larger than those through h-TMC$_6$. s-TMC$_6$ shows good permeance capability against hydrogen, while h-TMC$_6$ has low permeance capability for the different gas molecules. Specifically, in the temperature range of 100–300 K, the permeance values of H_2 through s-TMC$_6$ are always higher than the industrially acceptable one for gas separation. Meanwhile, the permeance values of CO_2 and CH_4 are always lower than the standard. For N_2 and CO, the permeance values will not be higher than the standard until the temperature is higher than 300 K. It is suggested that s-TMC$_6$ could be a potential H_2 purification membrane to separate H_2 from a mixture composed of N_2, CO, CO_2, or CH_4 below room temperature (100–300 K).
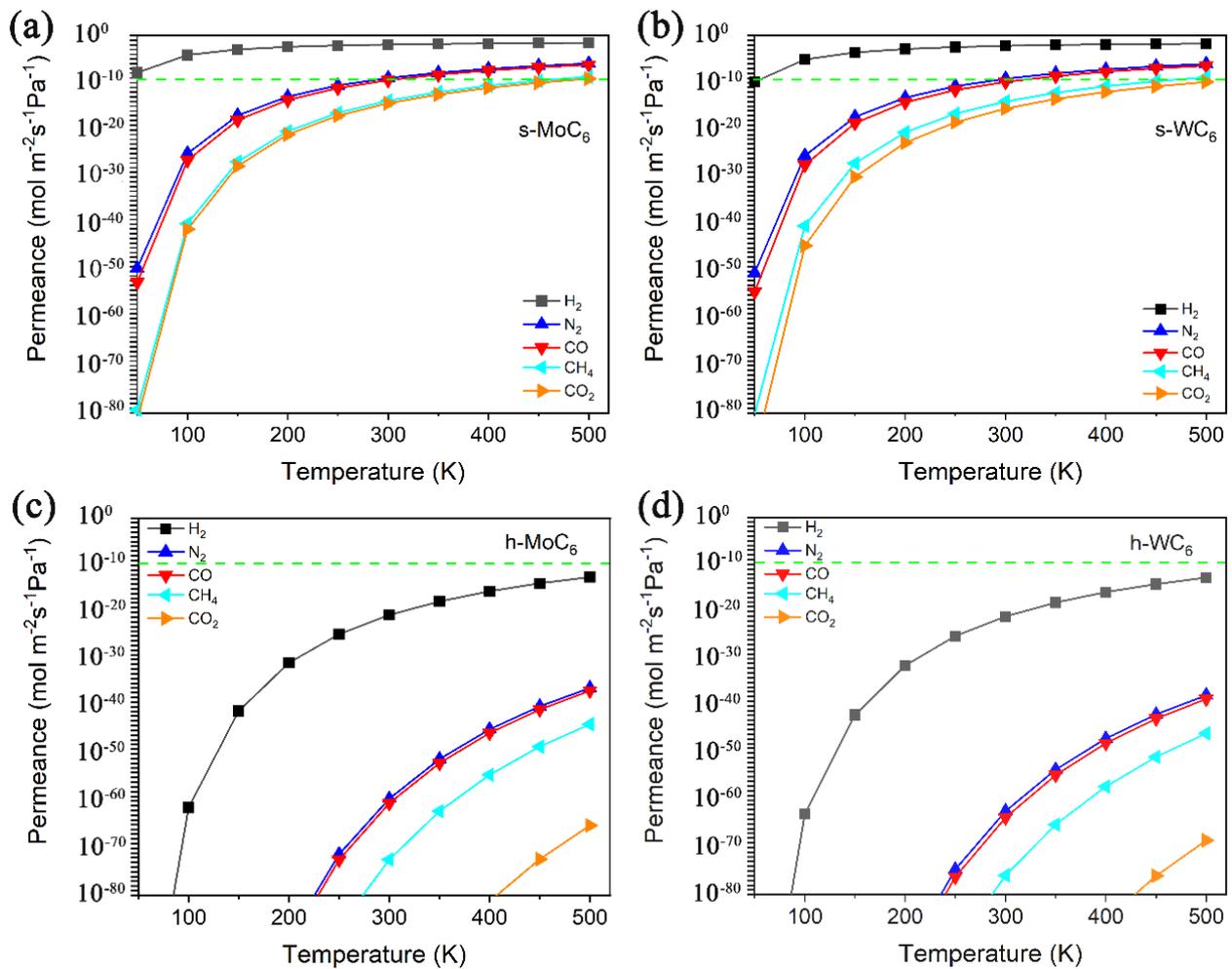
Figure 4. Permeance versus temperature for H_2, N_2, CO, CO_2, and CH_4 passing through the intrinsic pore of (**a**) s-MoC$_6$, (**b**) s-WC$_6$, (**c**) h-MoC$_6$, and (**d**) h-WC$_6$.

It is well accepted that the performance of a separation membrane is characterized by both the permeance capability and selectivity. Herein, the selectivity between two gas species is defined as the ratio of the diffusion rates, $S_{\text{gas-1/gas-2}} = A_{\text{gas-1}}/A_{\text{gas-2}}$, which comes from the Arrhenius equation:

$$A = A_0 exp(-E_b/k_B T) \qquad (4)$$

In Equation (2), the A_0 means the diffusion prefactor that can be taken as the same value for all gases (10^{11} s^{-1}). Based on the definition, the selectivity gradually decreases with the increase in temperature. In Figure 5, the selectivity versus temperature for H_2/N_2, H_2/CO, H_2/CH_4, and H_2/CO_2 separation by s-MoC$_6$ and s-WC$_6$ are illustrated. It is easy to find that the s-TMC$_6$ membranes mainly exhibit excellent selectivity for H_2/CH_4 and H_2/CO_2 due to the great differences in E$_b$ between H_2 and CH_4/CO_2. Different from other carbon-based 2D membranes, under room temperature (300 K), the selectivity of s-TMC$_6$ for H_2 against other gas molecules is not ideal enough, with 10^{11} and 10^{13} for H_2/CH_4 and H_2/CO_2, respectively. It is suggested that s-TMC$_6$ could be applied as H_2 purification membranes under low temperatures (100–250 K), with the selectivity of $H_2/(CO_2, CH_4)$ larger than 10^{15}. As indicated by the selectivity, s-WC$_6$ possesses better H_2 purification ability when compared with s-MoC$_6$.
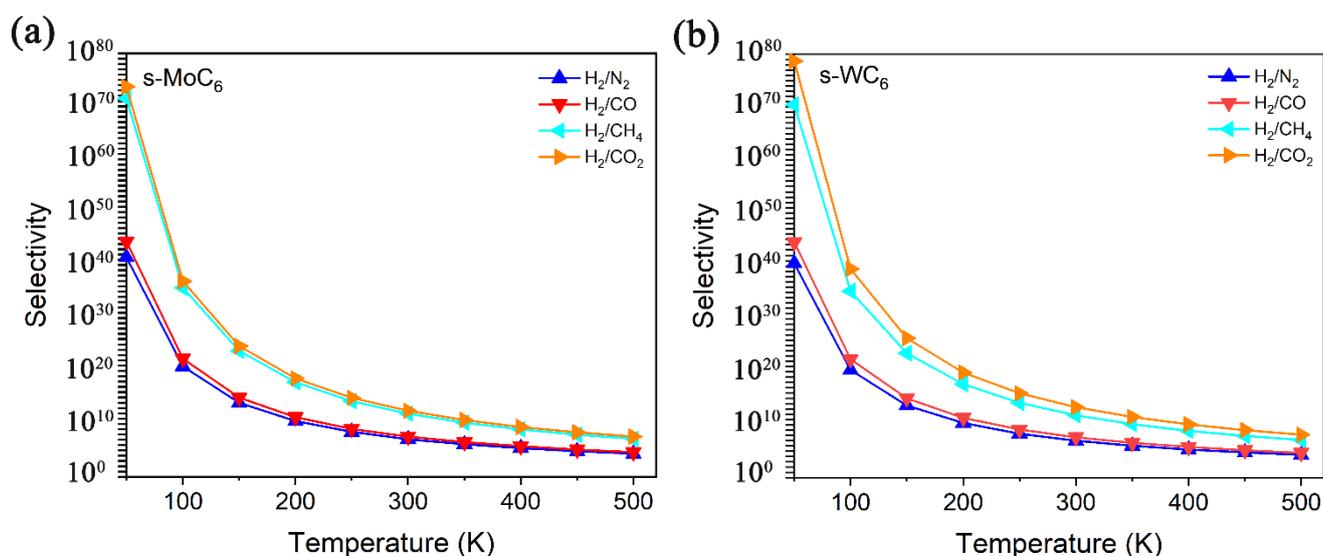
Figure 5. Selectivity versus temperature for H_2/N_2, H_2/CO, H_2/CH_4, and H_2/CO_2 separation by (**a**) s-MoC$_6$, (**b**) s-WC$_6$.

The convection–diffusion process is a problem in the field of fluid mechanics. Generally, the finite difference method (FDM) is a major method to treat with the convection–diffusion equation [25] which only applies to macroscopic systems. However, for microscopic systems such as the TMC$_6$ membranes in this work, it is extremely difficult to perform quantitative calculations on convection and diffusion of gas flow. As a result, the MD simulations were widely adopted to visualize the time-dependence diffusion process of the molecules, as well as to assess some parameters such as gas diffusion coefficient and the permeated number of gas molecules [26–29]. Due to the lack of quantitative results, MD simulations are often applied to confirm the results of DFT calculations.

To better understand the transmembrane processes during gas separation, we performed classical MD simulations (at 250 K) on the permeation of gas mixture through the TMC$_6$ membranes. During the MD simulations, a box of about 4 nm × 4 nm × 12 nm was employed; then, 60 H_2, 60 CO_2, and 60 CH_4 molecules were randomly put into a chamber composed of two TMC$_6$ membranes (the distance between the membranes was set as 4 nm). In Figure 6a,b, the number of permeated H_2 molecules versus the simulation time for gas mixture in the chamber composed of s-TMC$_6$ are depicted. It is found that after MD simulations of 5000 ps, there are 35 and 40 H_2 molecules diffusing outside of the s-MoC$_6$ and s-WC$_6$ membranes, respectively. It is worth noting that the diffusion equilibrium was not achieved within 5000 ps; we can expect that after a long enough time, all the H_2 molecules will diffuse through the s-TMC$_6$ membranes into the product chamber. The snapshots of the gas mixture permeating through the s-TMC$_6$ membranes at 0 ps, 500 ps, 1000 ps, and 5000 ps are given in Figure 6c,d. During the permeation process, the H_2 molecules gradually migrate from the feed chamber to the product chamber. Moreover, none of CO_2 or CH_4 is found outside the membranes, clearly indicating that the s-TMC$_6$ membranes could efficiently separate H_2 molecules from the H_2, CO_2, and CH_4 mixture. Therefore, the MD simulations could well simulate the transmembrane processes of H_2 molecules, which greatly supports our first-principle calculation results.

In addition, it should be mentioned that we also performed the same MD simulations on h-TMC$_6$. However, there are no gas molecules that run out from the chamber after 5000 ps at 250 K, indicating that h-TMC$_6$ could not work as effective gas separation membranes.
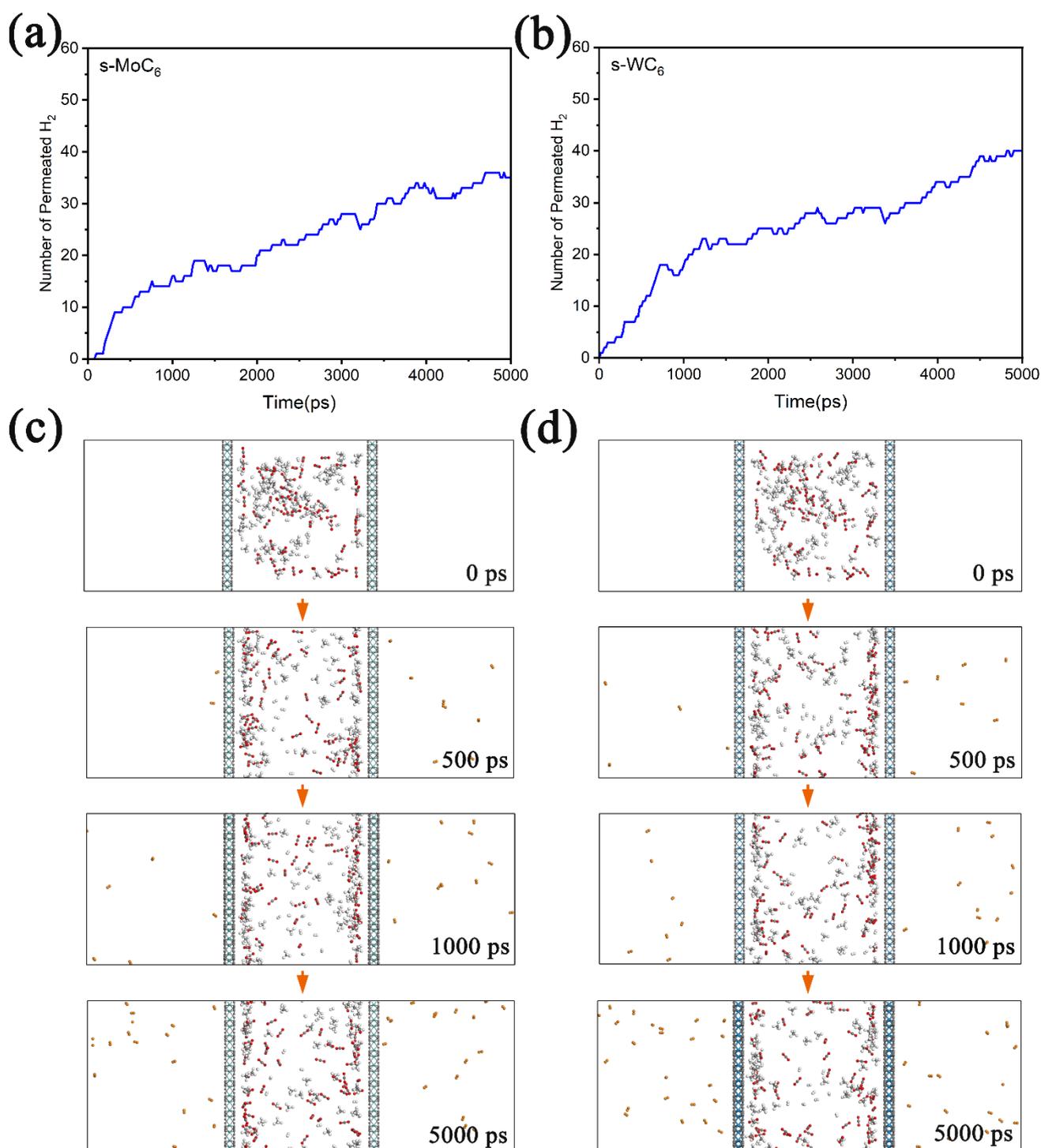
Figure 6. The number of permeated H_2 molecules versus the simulation time for gas mixture in chamber composed of (**a**) s-MoC$_6$ membranes and (**b**) s-WC$_6$ membranes. Corresponding snapshots of the diffusion process (from 0 to 5000 ps) of gas mixture permeating through (**c**) s-MoC$_6$ membranes and (**d**) s-WC$_6$ membranes. The H_2 molecules that diffuse outside are displayed by different color.

4. Conclusions

In this work, the potential applications of holey TMC$_6$ membranes in H_2 purification were uncovered by comparative first-principle calculations. The adsorption and diffusion behaviors of five gas molecules (including H_2, N_2, CO, CO_2, and CH_4) were investigated on h-TMC$_6$ and s-TMC$_6$. All the studied gas molecules showed weak physisorption on

the TMC_6 membranes, but distinguishing diffusion barriers were obtained for different gas molecules across the pores of TMC_6 membranes. The smaller pore size makes the gas molecules much more difficult to permeate into h-TMC_6 rather than into s-TMC_6. With suitable pore sizes, the s-TMC_6 structures not only show an extremely low diffusion barrier and acceptable permeance for the H_2 but also exhibit considerably high selectivity for H_2/CH_4 and H_2/CO_2, under relatively low temperature (150–250 K). Moreover, classical MD simulations on the permeation process also validated that the s-TMC_6 could effectively separate H_2 from the gas mixture composed of H_2, CO_2, and CH_4. Therefore, s-MoC_6 and s-WC_6 are qualified as separation membranes for H_2 purification from a gas mixture consisting of H_2, CH_4, and CO_2 below room temperature.

Institutional Review Board Statement: Not applicable.

Informed Consent Statement: Not applicable.

Conflicts of Interest: The authors declare no conflict of interest.

References

1. Wang, X.; Maeda, K.; Thomas, A.; Takanabe, K.; Xin, G.; Carlsson, J.M.; Domen, K.; Antonietti, M. A metal-free polymeric photocatalyst for hydrogen production from water under visible light. *Nat. Mater.* **2009**, *8*, 76–80. [CrossRef] [PubMed]
2. Höök, M.; Tang, X. Depletion of fossil fuels and anthropogenic climate change—A review. *Energy Policy* **2013**, *52*, 797–809. [CrossRef]
3. Unlu, D.; Hilmioglu, N.D. Application of aspen plus to renewable hydrogen production from glycerol by steam reforming. *Int. J. Hydrogen Energy* **2020**, *45*, 3509–3515. [CrossRef]
4. Ockwig, N.W.; Nenoff, T.M. Membranes for Hydrogen Separation. *Chem. Rev.* **2007**, *107*, 4078–4110. [CrossRef] [PubMed]
5. Jiao, Y.; Du, A.; Smith, S.C.; Zhu, Z.; Qiao, S.Z. H_2 purification by functionalized graphdiyne—Role of nitrogen doping. *J. Mater. Chem. A* **2015**, *3*, 6767–6771. [CrossRef]
6. Wang, Z.; Dong, H.; Yu, X.; Ji, Y.; Hou, T.; Li, Y. Two-dimensional porous polyphthalocyanine (PPc) as an efficient gas-separation membrane for ammonia synthesis. *Curr. Appl. Phys.* **2017**, *17*, 1765–1770. [CrossRef]
7. Wang, S.; Dai, S.; Jiang, D.-E. Continuously Tunable Pore Size for Gas Separation via a Bilayer Nanoporous Graphene Membrane. *ACS Appl. Nano Mater.* **2018**, *2*, 379–384. [CrossRef]
8. Ji, Y.; Dong, H.; Lin, H.; Zhang, L.; Hou, T.; Li, Y. Heptazine-based graphitic carbon nitride as an effective hydrogen purification membrane. *RSC Adv.* **2016**, *6*, 52377–52383. [CrossRef]
9. Li, F.; Qu, Y.; Zhao, M. Efficient helium separation of graphitic carbon nitride membrane. *Carbon* **2015**, *95*, 51–57. [CrossRef]
10. Zhu, L.; Xue, Q.; Li, X.; Wu, T.; Jin, Y.; Xing, W. C_2N: An excellent two-dimensional monolayer membrane for He separation. *J. Mater. Chem. A* **2015**, *3*, 21351–21356. [CrossRef]
11. Wang, Y.; Li, J.; Yang, Q.; Zhong, C. Two-Dimensional Covalent Triazine Framework Membrane for Helium Separation and Hydrogen Purification. *ACS Appl. Mater. Interfaces* **2016**, *8*, 8694–8701. [CrossRef] [PubMed]
12. Meng, Z.; Zhang, Y.; Shi, Q.; Liu, Y.; Du, A.; Lu, R. A remarkable two-dimensional membrane for multifunctional gas separation: Halogenated metal-free fused-ring polyphthalocyanine. *Phys. Chem. Chem. Phys.* **2018**, *20*, 18931–18937. [CrossRef] [PubMed]
13. Ning, C.; Zhang, Y.; Wang, J.; Gao, H.; Xiao, C.; Meng, Z.; Dong, H. Theoretically designed two-dimensional gamma-C_4O as an effective gas separation membrane for hydrogen purification. *Phys. Chem. Chem. Phys.* **2020**, *22*, 19492–19501. [CrossRef]
14. Li, X.; Dai, Y.; Ma, Y.; Sun, Q.; Wei, W.; Huang, B. Exotic quantum spin Hall effect and anisotropic spin splitting in carbon based TMC_6 (TM = Mo, W) kagome monolayers. *Carbon* **2016**, *109*, 788–794. [CrossRef]

15. Liu, P.F.; Wu, Y.; Bo, T.; Hou, L.; Xu, J.; Zhang, H.J.; Wang, B.T. Square transition-metal carbides MC6 (M = Mo, W) as stable two-dimensional Dirac cone materials. *Phys. Chem. Chem. Phys.* **2018**, *20*, 732–737. [CrossRef]

16. Kresse, G.; Furthmüller, J. Efficient iterative schemes for ab initio total-energy calculations using a plane-wave basis set. *Phys. Rev. B* **1996**, *54*, 11169–11186. [CrossRef]

17. Kresse, G.; Joubert, D. From ultrasoft pseudopotentials to the projector augmented-wave method. *Phys. Rev. B* **1999**, *59*, 1758–1775. [CrossRef]

18. Blöchl, P.E. Projector augmented-wave method. *Phys. Rev. B* **1994**, *50*, 17953–17979. [CrossRef]

19. Perdew, J.P.; Burke, K.; Ernzerhof, M. Generalized Gradient Approximation Made Simple. *Phys. Rev. Lett.* **1996**, *77*, 3865–3868. [CrossRef]

20. Monkhorst, H.J.; Pack, J.D. Special points for Brillouin-zone integrations. *Phys. Rev. B* **1976**, *13*, 5188–5192. [CrossRef]

21. Grimme, S.; Antony, J.; Ehrlich, S.; Krieg, H. A consistent and accurate ab initio parametrization of density functional dispersion correction (DFT-D) for the 94 elements H-Pu. *J. Chem. Phys.* **2010**, *132*, 154104. [CrossRef] [PubMed]

22. Henkelman, G.; Uberuaga, B.P.; Jónsson, H. A climbing image nudged elastic band method for finding saddle points and minimum energy paths. *J. Chem. Phys.* **2000**, *113*, 9901–9904. [CrossRef]

23. Rappe, A.K.; Casewit, C.J.; Colwell, K.S.; Goddard, W.A.; Skiff, W.M. UFF, a full periodic table force field for molecular mechanics and molecular dynamics simulations. *J. Am. Chem. Soc.* **1992**, *114*, 10024–10035. [CrossRef]

24. Blankenburg, S.; Bieri, M.; Fasel, R.; Müllen, K.; Pignedoli, C.A.; Passerone, D. Porous Graphene as an Atmospheric Nanofilter. *Small* **2010**, *6*, 2266–2271. [CrossRef]

25. Li, C. Finite Difference Method for Convection-Diffusion Equation. In *Computing and Data Science*; Cao, W., Ozcan, A., Xie, H., Guan, B., Eds.; Springer Nature: Singapore, 2021; pp. 193–203.

26. Wang, M.; Wang, Z.; Zhou, S.; Wang, J.; Liu, S.; Wei, S.; Guo, W.; Lu, X. Strain-controlled carbon nitride: A continuously tunable membrane for gas separation. *Appl. Surf. Sci.* **2020**, *506*, 144675. [CrossRef]

27. Zheng, H.; Zhu, L.; He, D.; Guo, T.; Li, X.; Chang, X.; Xue, Q. Two-dimensional graphene oxide membrane for H_2/CH_4 separation: Insights from molecular dynamics simulations. *Int. J. Hydrogen Energy* **2017**, *42*, 30653–30660. [CrossRef]

28. Jiang, C.; Hou, Y.; Wang, N.; Li, L.; Lin, L.; Niu, Q.J. Propylene/propane separation by porous graphene membrane: Molecular dynamic simulation and first-principle calculation. *J. Taiwan Inst. Chem. Eng.* **2017**, *78*, 477–484. [CrossRef]

29. Ding, L.; Wei, Y.; Li, L.; Zhang, T.; Wang, H.; Xue, J.; Ding, L.X.; Wang, S.; Caro, J.; Gogotsi, Y. MXene molecular sieving membranes for highly efficient gas separation. *Nat. Commun.* **2018**, *9*, 155. [CrossRef]